Chiral Topological Superconductivity in Superconductor-Obstructed Atomic Insulator-Ferromagnetic Insulator Heterostructures

Jingnan Hu,[1,*] Fei Yu,[1,*] Aiyun Luo,[1] Xiao-Hong Pan,[1] Jinyu Zou,[1] Xin Liu,[1,2,3] and Gang Xu[1,2,3,†]
[1]Wuhan National High Magnetic Field Center and School of Physics, Huazhong University of Science and Technology, Wuhan 430074, China
[2]Institute for Quantum Science and Engineering, Huazhong University of Science and Technology, Wuhan 430074, China
[3]Wuhan Institute of Quantum Technology, Wuhan 430206, China

(Received 15 January 2023; accepted 8 December 2023; published 16 January 2024)

Implementing topological superconductivity (TSC) and Majorana states (MSs) is one of the most significant and challenging tasks in both fundamental physics and topological quantum computations. In this work, taking the obstructed atomic insulator (OAI) Nb_3Br_8, s-wave superconductor (SC) $NbSe_2$, and ferromagnetic insulator (FMI) CrI_3 as an example, we propose a new setup to realize the 2D chiral TSC and MSs in the SC/OAI/FMI heterostructure, which could avoid the subband problem effectively and has the advantage of huge Rashba spin-orbit coupling. As a result, the TSC phase can be stabilized in a wide region of chemical potential and Zeeman splitting, and four distinct TSC phases with superconducting Chern number $\mathcal{N} = -1, -2, -3, 3$ can be achieved. Moreover, a 2D Bogoliubov–de Gennes Hamiltonian based on the triangular lattice of obstructed Wannier charge centers, combined with the s-wave superconductivity paring and Zeeman splitting, is constructed to understand the whole topological phase diagram analytically. These results expand the application of OAIs and pave a new way to realize the TSC and MSs with unique advantages.

DOI: 10.1103/PhysRevLett.132.036601

Topological superconductivity (TSC) has attracted intensive interest for its ability to host the Majorana states (MSs) and its implementation of topological quantum computations [1–19]. The initial system to realize TSC involves the p-wave pairing superconductor (SC) [20–24]. However, intrinsic p-wave SCs are very rare and MSs have not been clearly distinguished in these systems. In the past decade, many proposals have been raised to induce TSC at the surface or interface of the topological materials [25–30], semiconductors with Rashba spin-orbit coupling (Rashba SOC) [31–36], or magnetic atom chains [37–41] by the proximity effect with the s-wave SC. Among them, one delicate proposal is to realize the TSC and MSs, including the Majorana zero modes (MZMs) and chiral MSs, in the 1D (nanowire) [32,33,36] and 2D [34,35] semiconductor/s-wave SC heterostructures by modulating the Rashba SOC, Zeeman splitting, and chemical potential elaborately to satisfy an odd number of subband occupation. Moreover, it is proposed that the chiral MSs are easier to realize non-Abelian quantum gate operations, which could be 10^3 faster than the currently existing quantum computation schemes [34,35,42].

Recently, many important advances have been made in the semiconductor/s-wave SC heterostructures [43–48]. However, many difficulties and challenges have also been encountered, mainly caused by the multiple subbands and rather small SOC [49–56]. The multiple subbands not only reduce the energy window of odd number subband occupation to reach the TSC phase [57], but also bring out many trivial low-energy Andreev bound states that mimic the Majorana conductance signals [58–65]. Meanwhile, the small Rashba-SOC splitting would affect the stability of s-wave superconducting pairs in the presence of Zeeman splitting and, thus, make a great limitation of experimental confirmation of MSs [66].

In this Letter, by constructing the s-wave SC-obstructed atomic insulator (OAI)-ferromagnetic insulator (FMI) heterostructure as shown in Fig. 1(a), we propose a new TSC setup that could avoid the subband problem, in which the 2D TSC could be achieved by incorporating obstructed surface states (OSSs) with s-wave pairing and Zeeman splitting. Generally, OAIs are one kind of insulators that contain the obstructed Wannier charge centers (OWCCs), which are mismatched with the atomic positions but pinned at the Wyckoff positions between two atoms. As a result, metallic surface states, referred as OSSs, should exist inevitably on the OAI's surface that crosses the OWCCs, though it is a topologically trivial insulator. Such OSSs are usually well separated from the bulk bands and exhibit considerable Rashba-SOC splitting due to the spontaneous inversion symmetry breaking at the surface or interface, as schematically shown in Figs. 1(a) and 1(b). Therefore, OSSs are good analogs to the 2D electron gas at the interface of semiconductor/SC heterostructures [67,68], with the advantage of avoiding the subband problem and reducing the fake MZMs greatly when they become

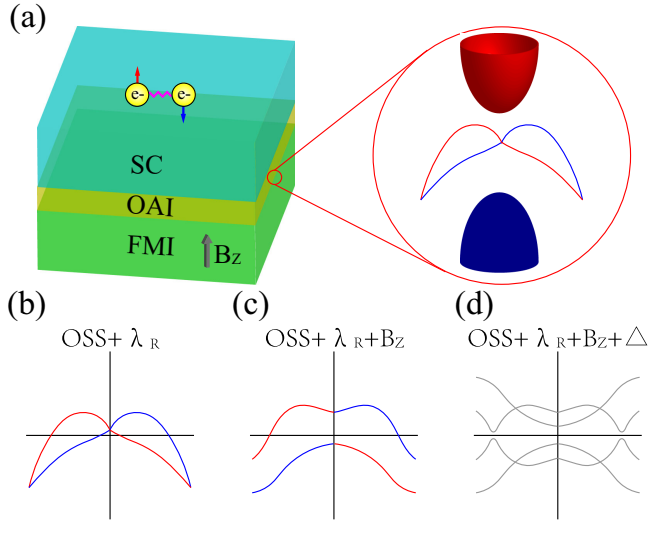

FIG. 1. (a) Schematic of the new chiral TSC setup based on SC/OAI/FMI heterostructure, where the bulk states of the OAI and the corresponding OSSs at the interface are illustrated in the red circle. (b) OSSs exhibit huge Rashba-SOC splitting. (c) The Kramers degeneracy of OSSs lifted by the out-of-plane Zeeman splitting B_z. (d) Illustration of the TSC spectrum realized on the OSSs incorporating the Zeeman splitting B_z and SC pairing Δ.

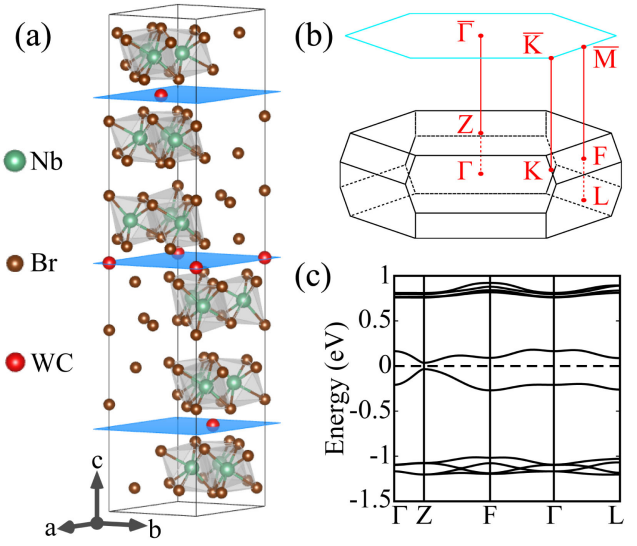

FIG. 2. (a) Crystal structure of Nb_3Br_8, where the red balls represent the positions of the OWCCs. The blue planes are the cleavage surfaces that cross the OWCCs. (b) High-symmetry points of the 3D BZ of the primitive cell Nb_3Br_8 and the projected 2D BZ on the (1, 1, 1) surface. (c) Bulk band structures with SOC along the high-symmetry paths of Nb_3Br_8.

TSC [64]. The out-of-plane Zeeman splitting will lift the Kramers degeneracy at the time-reversal invariant momentum points, which can lead to an odd number of Fermi surfaces (FSs) as shown in Fig. 1(c). Since opposite spins are locked at the opposite momentum of OSSs, *s*-wave pairing would be introduced into OSSs easily by the proximity effect, according to the Fu-Kane argument [25]. Consequently, it has a big chance to generate the TSC phase on such OSSs with superconducting pairing and Zeeman splitting as schematically shown in Fig. 1(d).

Here, we choose Nb_3Br_8 as a concrete example to verify the feasibility and advantages of our proposal. As shown in Fig. 2(a), Nb_3Br_8 is a van der Waals layered material that crystallizes in the 166 space group, where Wyckoff positions 6c and 18h are occupied by Nb and Br atoms, respectively, and its corresponding Brillouin zone (BZ) is plotted in Fig. 2(b) [69–71]. As reported in Refs. [72–74], Nb_3Br_8 is identified as an OAI with OWCCs located at empty Wyckoff position 3b as sketched by the red balls in Fig. 2(a). These OWCCs form the triangular lattice between the van der Waals layers as shown by the blue planes in Fig. 2(a). As a result, a natural cleavage surface of Nb_3Br_8 usually consists of such OWCCs, leading to 2D metallic OSSs at the surface or interface. Moreover, superconducting diode effects have been reported in the $NbSe_2/Nb_3Br_8/NbSe_2$ Josephson junctions recently [75], which indicates the possibility to introduce *s*-wave pairing into the OSSs at the interface of the experimentally synthesized $Nb_3Br_8/NbSe_2$ heterostructure.

By using the experimental crystal parameters [69], we perform the electronic structures calculations of Nb_3Br_8 based on the Vienna *ab initio* simulation package [76,77] with 500 eV energy cutoff, $9 \times 9 \times 9$ *k*-point grids, and the Perdew-Burke-Ernzerhof-type exchange-correlation potential [78]. The calculated band structures including SOC are plotted in Fig. 2(c), which gives rise to a 0.69 eV insulating gap, consistent with previous works very well [72]. By calculating the band representation at the maximal high-symmetry *k* points, we confirm that Nb_3Br_8 is a topologically trivial insulator and an OAI. To confirm the OAI character of Nb_3Br_8, we build a ten-layer slab and calculate the slab bands by WannierTools [79] based on the Wannier functions of the Nb-*d* orbits constructed by WANNIER90 [80]. The slab bands are plotted in Fig. 3(a), in which the metallic OSSs originated from the OWCCs on the surface always present at the Fermi level ($E_F = 0$), no matter whether SOC is considered or not. The OSS calculated without SOC is displayed in gray in Fig. 3(a), while the OSSs considering SOC are plotted by the color bar to represent spin $S_x = 1/2$ (red) and $S_x = -1/2$ (blue) components, respectively. These results manifest that the OSS on the surface of Nb_3Br_8 has a strong Rashba-SOC splitting, which can be estimated roughly by the band splitting between the OSSs with and without SOC. By measuring the energy difference of the OSS band maximum along the $\bar{\Gamma} - \bar{M}$ path as shown in Fig. 3(a), the amplitude of Rashba-SOC splitting ξ_{SO} is evaluated as about 6.7 meV, which is about one order larger than that in semiconductor InAs [49,50,52,55,56].

Such strong Rashba SOC will result in robust spin-momentum-locking OSSs. We calculate the spin textures of the FSs at 4 meV above the Fermi level E_F [green dotted

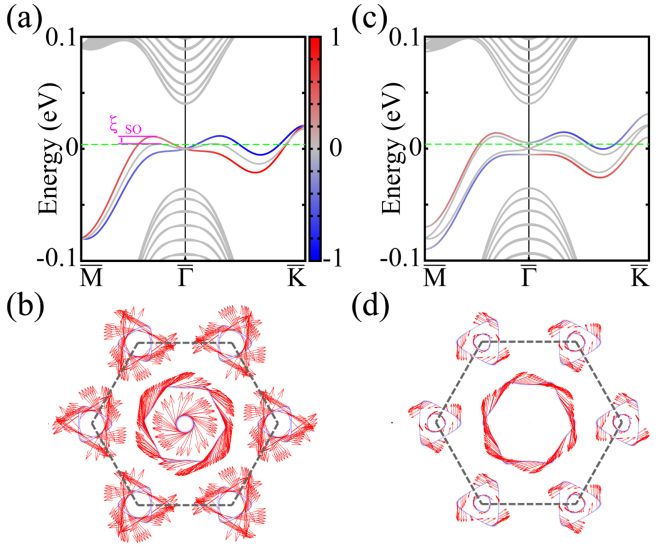

FIG. 3. (a) Band structures of ten-layer Nb_3Br_8 slab at $B_z = 0$, where OSS without SOC is plotted in gray and OSSs with SOC are plotted by the color bar to describe different spin S_x components. ξ_{SO} indicates the amplitude of Rashba-SOC splitting. (b) The spin textures on the FSs when the Fermi energy in (a) is set at 4 meV above E_F (green dotted line). (c) Band structures of ten-layer Nb_3Br_8 slab with 10 meV out-of-plane Zeeman splitting applied on the bottom layer. The gray OSSs and color OSSs are from the top layer and bottom layer, respectively. (d) Spin textures on the FSs when the Fermi energy in (c) is set at 4 meV above E_F.

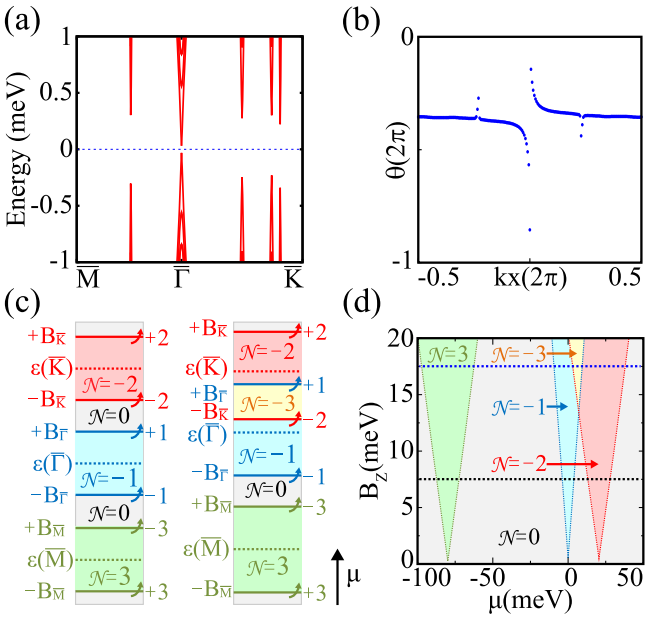

FIG. 4. (a) BdG spectrum of Nb_3Br_8 slab with $\mu = 0$, $B_z = 0.55$ meV, and $\Delta_{SC} = 1$ meV. (b) The corresponding Wilson loop evolution of all occupied states in (a), where θ is the Wannier charge center. (c) Illustration of the TSC phase evolution with μ increasing, where $B_{\bar{M},\bar{\Gamma},\bar{K}}$ mean the applied Zeeman splitting at the M̄, Γ̄, and K̄ points. The left and right panels correspond to the TSC evolution at weak and strong B_z situations, respectively, as illustrated by the black and blue dashed line in (d), respectively. (d) The calculated whole TSC phase diagram of the heterostructure in the space of B_z and μ by using $\Delta_{SC} = 1$ meV.

line in Fig. 3(a)], as plotted in Fig. 3(b), which reveals that the spins at opposite momentum are oriented oppositely due to the strong Rashba-SOC effect. We propose CrI_3, with a similar triangle lattice constant (6.87 Å) to Nb_3Br_8 (7.08 Å), as the FMI substrate to introduce the magnetic proximity. Generally, such magnetic proximity may bring two effects on the interface, i.e., orbital effect and Zeeman splitting. Through our analysis, orbital effects are negligible as shown in Sec. I in Supplemental Material [81]. So we consider only the Zeeman splitting in the following calculations. The CrI_3-induced Zeeman splitting is 7.7, 0.6, and 4.3 meV at the Γ̄, M̄, and K̄ point, respectively, as shown in Fig. S2 [81], which are similar to the calculations in Ref. [84]. We then added a Zeeman splitting $B_z = 10$ meV at the bottom layer of Nb_3Br_8 and found that OSSs still have sizable in-plane spin components as shown in Figs. 3(c) and 3(d), which implies that the superconductivity on the OSSs would be more stable against the Zeeman splitting due to huge Rashba-SOC effect as reported in [84,85].

We go further to investigate the TSC property of our setup shown in Fig. 1(a) by considering $NbSe_2$ ($\Delta_{SC} = 1$ meV) as the SC substrate and adopting the method developed in [86,87]. The layer-dependent superconducting gap [86] is used in OAI by adopting

$$\Delta_{OAI} = \Delta_{SC}\frac{\cosh[k(z-d)]}{\cosh[kd]}, \quad 0 < z < d,$$
$$k^2 = \frac{t}{\Xi_0}\left(\frac{t}{\Xi_0}+\frac{3}{l}\right), \tag{1}$$

where d is the thickness of OAI. The mean free path $l = 16$ nm [88], superconducting correlation length $\Xi_0 = 7.7$ nm [89], and $t = T/T_c = 0.6$ is set by fitting with the $NbSe_2/Bi_2Se_3$ heterostructure [88,90], giving rise to the effective pairing gap $\Delta_b = 0.25$ meV on the bottom OSSs for the ten-layer Nb_3Br_8, as shown in Fig. S4 [81]. In Fig. 4(a), the fully gapped low-energy spectrum of the Bogoliubov–de Gennes (BdG) Hamiltonian is obtained with chemical potential $\mu = 0$ and $B_z = 0.55$ meV, which is smaller than the upper critical field of layered $NbSe_2$ (about 0.58 meV [85]). Thus, the BdG Chern number $\mathcal{N}$ is well defined [91] and characterized by the winding number of the occupied BdG spectrum's Wilson loop [92–94], which gives $\mathcal{N} = -1$ as shown in Fig. 4(b). With B_z increasing, the TSC property maintains, while the BdG gap increases and

reaches a maximum value of 0.44 meV at $B_z = 0.9$ meV as shown in Fig. S4(b) [81]. These results verify the feasibility of our setup that chiral TSC can be achieved on the OSSs by incorporating s-wave pairing and tiny Zeeman splitting.

Now we discuss the TSC stability in our setup. First, since the magnetic proximity effect is dominated by the exchange coupling [95,96], which generally decays exponentially [97–99], spontaneous vortices could not be generated as studied in Refs. [98,100]. Second, it has been reported that strong Rashba SOC can enhance the stability of the superconductivity against the Zeeman splitting [85]. To confirm this conclusion, we study the spatial decay of the superconducting gap in SC/OAI/FMI heterostructures based on the TB model. The calculated results demonstrate that the superconducting gap induced by the proximity effect can exist stably even in the presence of Zeeman splitting with an order of magnitude larger than Δ_{SC} [81]. Moreover, the superconductivity has been reported to survive in $NbSe_2/CrBr_3$ heterostructure, which has similar Zeeman splitting to our setup but smaller Rashba-SOC splitting [84]. Therefore, the TSC in our setup should be more stable against the larger Zeeman splitting.

One can understand the TSC properties of the heterostructure through a 2D triangular lattice model analytically, since the OSSs are originated from the OWCCs that form the triangular lattice as sketched in Fig. 2(a). The 2D tight-binding model based on the triangular lattice with one orbital per site is constructed as the form of $\hat{H}_{SS} = \sum_{k,\sigma,\sigma'} c^{\dagger}_{k\sigma}[H_{SS}(k)]_{\sigma\sigma'} c_{k\sigma'}$ $(\sigma, \sigma' = \uparrow, \downarrow)$ and $H_{SS}(k) = \varepsilon(k) + \sum_{j=x,y} E_R^{(j)}(k)\sigma_j$ with

$$\begin{aligned}
\varepsilon(k) &= \varepsilon_1(k) + \varepsilon_2(k) + \varepsilon_3(k) - \varepsilon_0,\\
\varepsilon_1(k) &= -2t_1[\cos(2k_xL) + 2\cos(k_xL)\cos(\sqrt{3}k_yL)],\\
\varepsilon_2(k) &= -2t_2[\cos(2\sqrt{3}k_yL) + 2\cos(3k_xL)\cos(\sqrt{3}k_yL)],\\
\varepsilon_3(k) &= -2t_3[\cos(4k_xL) + 2\cos(2k_xL)\cos(2\sqrt{3}k_yL)],\\
E_R^x(k) &= 2\lambda_R\sqrt{3}\cos(k_xL)\sin(\sqrt{3}k_yL),\\
E_R^y(k) &= -2\lambda_R[\sin(2k_xL) + \sin(k_xL)\cos(\sqrt{3}k_yL)],
\end{aligned} \tag{2}$$

where σ_i $(i = x, y, z)$ are the Pauli matrices in the spin space. ε_0 is the on-site energy that can be contracted into the chemical potential in the subsequent BdG Hamiltonian. t_1, t_2, and t_3 are the hopping amplitudes of the nearest neighbor, next-nearest neighbor, and third-nearest neighbor, respectively. $L = a/2$ is length parameter described by the lattice constant a. $E_R^{x/y}(k)$ is the x/y component of the Rashba-SOC term with λ_R describing the strength of Rashba SOC. We use such an effective model to fit the numerically calculated OSS band structures of Nb_3Br_8 in Fig. 3(a) and obtain the fitted parameters as $t_1 = -5$ meV, $t_2 = -5$ meV, $t_3 = 7$ meV, and $\lambda_R = 2.5$ meV.

Taking the Zeeman splitting B_z and the SC pairing amplitude Δ_{b} into account, we can write out the total 2D effective Hamiltonian as $\hat{H} = \hat{H}_{SS} + \hat{H}_Z + \hat{H}_{\mathrm{SC}}$ with $\hat{H}_Z = \sum_{k,\sigma,\sigma'} c^{\dagger}_{k\sigma}[B_z\sigma_z]_{\sigma\sigma'} c_{k\sigma'}$ and $\hat{H}_{\mathrm{SC}} = \sum_k \Delta_{\mathrm{b}}(c^{\dagger}_{k\uparrow}c^{\dagger}_{-k\downarrow} + \mathrm{H.c.})$. Here, we set $B_z > 0$ without losing generality. In the Nambu basis $\Psi_k = (c_{k\uparrow}, c_{k\downarrow}, c^{\dagger}_{-k\uparrow}, c^{\dagger}_{-k\downarrow})^T$, this total Hamiltonian $\hat{H} = \frac{1}{2}\sum_k \Psi_k^{\dagger} H_{\mathrm{BdG}}(k)\Psi_k$ can be rewritten as

$$\begin{aligned}
H_{\mathrm{BdG}} = {} & \tau_z \otimes (E_T\sigma_0 + E_R^y\sigma_y + B_z\sigma_z)\\
& + E_R^x\tau_0 \otimes \sigma_x - \Delta_{\mathrm{b}}\tau_y \otimes \sigma_y,
\end{aligned} \tag{3}$$

where τ_i (σ_i) and τ_0 (σ_0) are the Pauli and identity matrices in the particle-hole (spin) space, respectively. $E_T(k) = \varepsilon(k) - \mu$, and μ is the chemical potential. By solving Eq. (2) analytically, it is straightforward to prove that the energy spectrum can be closed only at the high-symmetry points $\bar{\Gamma}$, $\bar{M}$, and $\bar{K}$ of the 2D BZ as shown in Fig. 2(b) [81]. Therefore, the topological phase transition can be determined only by the effective $k \cdot p$ model $\mathcal{H}_{\bar{\Gamma}}$, $\mathcal{H}_{\bar{M}}$, and $\mathcal{H}_{\bar{K}}$ by treating Δ_{b} as perturbation [101]. To do that, we first write the unperturbed Hamiltonian $\hat{H}_0 = \hat{H}_{SS} + \hat{H}_Z$, and its spectrum in Nambu basis is expressed as

$$\pm\varepsilon_{\pm}(k) = \pm[\varepsilon(k) - \mu \pm \delta\varepsilon(k)] \tag{4}$$

with $\delta\varepsilon = \sqrt{(E_R^x)^2 + (E_R^y)^2 + B_z^2}$. $\chi_1^{\pm} = (E_R^x - iE_R^y, \pm\delta\varepsilon - B_z, 0, 0)^T/N$ and $\chi_2^{\pm} = (0, 0, -E_R^x - iE_R^y, \pm\delta\varepsilon - B_z)^T/N$ are the eigenvectors corresponding to $\varepsilon_{\pm}$ and $-\varepsilon_{\pm}$, respectively, with the normalization factor $N = \sqrt{2\delta\varepsilon(\delta\varepsilon \mp B_z)}$. In the following, we will construct the effective $k \cdot p$ model near the high-symmetry points with the perturbation of Δ_{b}, to demonstrate the system's TSC properties.

We first construct the effective model near $\bar{\Gamma}$ point to explain the TSC phase realized in Figs. 4(a) and 4(b). By setting the Zeeman splitting as a fixed value $B_{\bar{\Gamma}}$, the topological phase transition would be controlled just by the chemical potential μ [102]. The gap-closing condition at $\bar{\Gamma}$ point $\varepsilon_{\pm}(\bar{\Gamma}) = 0$ divides the whole chemical potential into two distinct topological regions: the light blue area satisfying $\varepsilon(\bar{\Gamma}) + B_{\bar{\Gamma}} > \mu > \varepsilon(\bar{\Gamma}) - B_{\bar{\Gamma}}$ as shown in Fig. 4(c) and the region otherwise. While the latter chemical potential region gives rise to the topologically trivial SC, TSC phase can be realized in the light blue area [102], in which the two lowest eigenvectors $\chi_{1,2}^-$ are used to derive the minimal Hamiltonian as $[\mathcal{H}_{\bar{\Gamma}}]_{\alpha\beta} = \langle\chi_{\alpha}^-|(\hat{H}_0 + \hat{H}_{\mathrm{SC}})|\chi_{\beta}^-\rangle$ $(\alpha, \beta = 1, 2)$. Finally, we obtain

$$\mathcal{H}_{\bar{\Gamma}}(k) = -\tilde{\Delta}(k_x\sigma_x - k_y\sigma_y) + \left(\frac{1}{2m_{\bar{\Gamma}}}k^2 - \mu_{\bar{\Gamma}}\right)\sigma_z \tag{5}$$

with $k^2 = k_x^2 + k_y^2$. Equation (5) is a canonical 2D chiral p-wave superconductivity model with $\tilde{\Delta} = 3a\Delta_{\mathrm{b}}\lambda_R/B_z$, $\mu_{\bar{\Gamma}} = \mu - \varepsilon(\bar{\Gamma}) + B_{\bar{\Gamma}}$, and $m_{\bar{\Gamma}} = 1/3a^2(t_1 + 3t_2 + 4t_3) > 0$, which gives rise to a $\mathcal{N} = -1$ TSC phase according to the

definition of the SC Chern number $\mathcal{N} = -(\mathrm{sgn}[m_{\bar{\Gamma}}] + \mathrm{sgn}[\mu_{\bar{\Gamma}}])/2$ [103]. Thus, Eq. (5) well explains the TSC physics when the chemical potential is set near the $\bar{\Gamma}$ point ($\mu = 0$), i.e., the TSC phase realized in Figs. 4(a) and 4(b). More derivation details can be seen in Sec. III, and the chiral Majorana edge modes are calculated and presented in Sec. IV in Supplemental Material [81].

Similar discussion can be made at $\bar{\mathrm{M}}$ and $\bar{\mathrm{K}}$ points. The gap-closing condition near $\bar{\mathrm{M}}$ point $\varepsilon_{\pm}(\bar{\mathrm{M}}) = 0$ will give the TSC phase area enclosed by $\mu = \varepsilon(\bar{\mathrm{M}}) \pm B_{\bar{\mathrm{M}}}$ [light green area in Fig. 4(c)], where $B_{\bar{\mathrm{M}}}$ is the fixed Zeeman splitting at the $\bar{\mathrm{M}}$ point. By using two lowest eigenvectors $\chi^{-}_{1,2}$, the minimal model in the light green area can be deduced as $\mathcal{H}_{\bar{\mathrm{M}}}(k) = -\tilde{\Delta}(k_x\sigma_x + k_y\sigma_y) + [1/(2m^x_{\bar{\mathrm{M}}})k^2 + 1/(2m^y_{\bar{\mathrm{M}}})k^2 - \mu_{\bar{\mathrm{M}}}]\sigma_z$, with $\mu_{\bar{\mathrm{M}}} = \mu - \varepsilon(\bar{\mathrm{M}}) + B_{\bar{\mathrm{M}}}$, $m^x_{\bar{\mathrm{M}}} = 1/a^2(t_1 - 9t_2 + 12t_3) > 0$, and $m^y_{\bar{\mathrm{M}}} = 1/3a^2(-t_1 + t_2 + 4t_3) > 0$, which is obversely a chiral p-wave SC with $\mathcal{N} = 1$. Moreover, since the Berry curvatures near three $\bar{\mathrm{M}}$ points accumulate with each other [84], $\mathcal{N} = 3$ topological phase is realized in this area. At $\bar{\mathrm{K}}$ points, the lowest eigenvectors become $\chi^{+}_{1,2}$ to determine the topological phase in the red area enclosed by $\mu = \varepsilon(\bar{\mathrm{K}}) \pm B_{\bar{\mathrm{K}}}$ in Fig. 4(c) with $B_{\bar{\mathrm{K}}}$ as the fixed Zeeman splitting at the $\bar{\mathrm{K}}$ point. The $k \cdot p$ Hamiltonian is, thus, given as $\mathcal{H}_{\bar{\mathrm{K}}}(k) = -\tilde{\Delta}/2(k_x\sigma_x + k_y\sigma_y) + [(1/2m_{\bar{\mathrm{K}}})k^2 - \mu_{\bar{\mathrm{K}}}]\sigma_z$, with $\mu_{\bar{\mathrm{K}}} = \mu - \varepsilon(\bar{\mathrm{K}}) - B_{\bar{\mathrm{K}}}$ and $m_{\bar{\mathrm{K}}} = 2/3a^2(-t_1 + 6t_2 - 4t_3) < 0$, which gives rise to SC Chern number -1 at each $\bar{\mathrm{K}}$ point. Since there are two equivalent $\bar{\mathrm{K}}$ points, $\mathcal{N} = -2$ TSC phase is realized in the red area finally.

According to the energy arrangement of the $\bar{\Gamma}$, $\bar{\mathrm{M}}$, and $\bar{\mathrm{K}}$ shown in Figs. 3(a) and 3(c), the TSC phase should evolute with μ increasing as illustrated in the left panel in Fig. 4(c), where three TSC phases determined by $\mathcal{H}_{\bar{\Gamma}}$, $\mathcal{H}_{\bar{M}}$, and $\mathcal{H}_{\bar{K}}$ are well separated from each other, corresponding to the weak B_z situation. Thus, we can tune the chemical potential μ to get three different TSC phases. Moreover, if the applied B_z is strong enough so that the areas overlap, an extra TSC phase with $\mathcal{N} = -3$ will emerge as suggested by the yellow area in the right panel in Fig. 4(c).

In Fig. 4(d), we further numerically calculated the whole TSC phase diagram of the heterostructure as a function of μ and B_z by using the same parameters in the calculations in Figs. 4(a) and 4(b), which agree with our model analysis very well except that the TSC phase can be obtained only when the Zeeman splitting at $\bar{\Gamma}$, $\bar{\mathrm{M}}$, and $\bar{\mathrm{K}}$ exceeds 0.5, 0.25, and 0.5 meV, respectively. This is because the effective Zeeman gap should surpass the energy of Δ_b at least to achieve a nontrivial SC Chern number [34]. Finally, it is also worth noticing that some in-gap segmented FSs will appear in the $\bar{\Gamma} - \bar{\mathrm{K}}$ path due to the Ising-type SOC at large Zeeman splitting B_z, as reported in Ref. [104].

Conclusion and discussion.—We have proposed a new setup to realize the 2D chiral TSC in the SC/OAI/FMI heterostructure, which mainly has two advantages. First, our scheme is subband-free, which will greatly reduce the fake Majorana state problem [64]. Second, the strong Rashba SOC of OSSs improves the stability of superconductivity and also provides a wider chemical potential window for the TSC. These advantages greatly enhance the experimental feasibility of detecting and controlling MZMs. To verify our scheme, we consider the $NbSe_2/Nb_3Br_8/CrI_3$ as a concrete example. The calculations unveil the $\mathcal{N} = -1$ TSC achieved by the natural carrier filling interface ($\mu = 0$) with $B_z > 0.5$ meV. Moreover, we also construct a 2D effective BdG model based on the triangular lattice of OWCCs, and the whole TSC phase diagram in the space of μ and B_z is figured out analytically, which demonstrates that four distinct TSC phases with SC Chern numbers $\mathcal{N} = -1, -2, -3, 3$ can be achieved in the whole μ and B_z space. These results provide OAIs as a new platform to design the chiral TSC and MSs, which will stimulate more interest from both TSC and OAI studies, especially studies on $NbSe_2/Nb_3Br_8$ heterostructure [75].

We thank Xi Dai and Biao Lian for helpful discussions. This work is supported by the National Natural Science Foundation of China (12274154).

*These authors contributed equally to this work.
†gangxu@hust.edu.cn

[1] E. Majorana, Il Nuovo Cimento (1924–1942) **14**, 171 (1937).
[2] N. Read and D. Green, Phys. Rev. B **61**, 10267 (2000).
[3] D. A. Ivanov, Phys. Rev. Lett. **86**, 268 (2001).
[4] A. Y. Kitaev, Phys. Usp. **44**, 131 (2001).
[5] S. B. Bravyi and A. Y. Kitaev, Ann. Phys. (Amsterdam) **298**, 210 (2002).
[6] H.-Y. Fan, H.-L. Lu, and Y. Fan, Ann. Phys. (Amsterdam) **321**, 480 (2006).
[7] J. D. Sau, D. J. Clarke, and S. Tewari, Phys. Rev. B **84**, 094505 (2011).
[8] J. Alicea, Rep. Prog. Phys. **75**, 076501 (2012).
[9] F. Zhang, C. L. Kane, and E. J. Mele, Phys. Rev. Lett. **111**, 056402 (2013).
[10] S. A. Yang, H. Pan, and F. Zhang, Phys. Rev. Lett. **113**, 046401 (2014).
[11] G. Xu, J. Wang, B. Yan, and X.-L. Qi, Phys. Rev. B **90**, 100505(R) (2014).
[12] T. Kawakami and X. Hu, Phys. Rev. Lett. **115**, 177001 (2015).
[13] Q. Wang, C.-C. Liu, Y.-M. Lu, and F. Zhang, Phys. Rev. Lett. **121**, 186801 (2018).
[14] R.-X. Zhang, W. S. Cole, and S. Das Sarma, Phys. Rev. Lett. **122**, 187001 (2019).
[15] R.-X. Zhang, W. S. Cole, X. Wu, and S. Das Sarma, Phys. Rev. Lett. **123**, 167001 (2019).

[16] R.-X. Zhang and S. Das Sarma, Phys. Rev. Lett. **126**, 137001 (2021).
[17] J. Zou, Q. Xie, Z. Song, and G. Xu, Natl. Sci. Rev. **8**, nwaa169 (2021).
[18] R. Giwa and P. Hosur, Phys. Rev. Lett. **127**, 187002 (2021).
[19] G. Margalit, B. Yan, M. Franz, and Y. Oreg, Phys. Rev. B **106**, 205424 (2022).
[20] Y. Maeno, H. Hashimoto, K. Yoshida, S. Nishizaki, T. Fujita, J. Bednorz, and F. Lichtenberg, Nature (London) **372**, 532 (1994).
[21] K. Nelson, Z. Mao, Y. Maeno, and Y. Liu, Science **306**, 1151 (2004).
[22] Y. S. Hor, A. J. Williams, J. G. Checkelsky, P. Roushan, J. Seo, Q. Xu, H. W. Zandbergen, A. Yazdani, N. P. Ong, and R. J. Cava, Phys. Rev. Lett. **104**, 057001 (2010).
[23] L. Jiao, S. Howard, S. Ran, Z. Wang, J. O. Rodriguez, M. Sigrist, Z. Wang, N. P. Butch, and V. Madhavan, Nature (London) **579**, 523 (2020).
[24] B.-X. Li and Z. Yan, Phys. Rev. B **103**, 064512 (2021).
[25] L. Fu and C. L. Kane, Phys. Rev. Lett. **100**, 096407 (2008).
[26] P. Hosur, P. Ghaemi, R. S. K. Mong, and A. Vishwanath, Phys. Rev. Lett. **107**, 097001 (2011).
[27] G. Xu, B. Lian, P. Tang, X.-L. Qi, and S.-C. Zhang, Phys. Rev. Lett. **117**, 047001 (2016).
[28] Y. Peng and Y. Xu, Phys. Rev. B **99**, 195431 (2019).
[29] X.-H. Pan, K.-J. Yang, L. Chen, G. Xu, C.-X. Liu, and X. Liu, Phys. Rev. Lett. **123**, 156801 (2019).
[30] W. Liu, A. Luo, G. Zhong, J. Zou, and G. Xu, Phys. Rev. Res. **4**, 023127 (2022).
[31] M. Sato, Y. Takahashi, and S. Fujimoto, Phys. Rev. Lett. **103**, 020401 (2009).
[32] R. M. Lutchyn, J. D. Sau, and S. Das Sarma, Phys. Rev. Lett. **105**, 077001 (2010).
[33] Y. Oreg, G. Refael, and F. von Oppen, Phys. Rev. Lett. **105**, 177002 (2010).
[34] J. D. Sau, R. M. Lutchyn, S. Tewari, and S. Das Sarma, Phys. Rev. Lett. **104**, 040502 (2010).
[35] J. Alicea, Phys. Rev. B **81**, 125318 (2010).
[36] T. D. Stanescu, R. M. Lutchyn, and S. Das Sarma, Phys. Rev. B **84**, 144522 (2011).
[37] S. Nadj-Perge, I. K. Drozdov, B. A. Bernevig, and A. Yazdani, Phys. Rev. B **88**, 020407(R) (2013).
[38] J. Klinovaja, P. Stano, A. Yazdani, and D. Loss, Phys. Rev. Lett. **111**, 186805 (2013).
[39] Y. Kim, M. Cheng, B. Bauer, R. M. Lutchyn, and S. Das Sarma, Phys. Rev. B **90**, 060401(R) (2014).
[40] J. Li, H. Chen, I. K. Drozdov, A. Yazdani, B. A. Bernevig, and A. H. MacDonald, Phys. Rev. B **90**, 235433 (2014).
[41] M. M. Glazov, T. Amand, X. Marie, D. Lagarde, L. Bouet, and B. Urbaszek, Phys. Rev. B **89**, 201302(R) (2014).
[42] B. Lian, X.-Q. Sun, A. Vaezi, X.-L. Qi, and S.-C. Zhang, Proc. Natl. Acad. Sci. U.S.A. **115**, 10938 (2018).
[43] V. Mourik, K. Zuo, S. M. Frolov, S. Plissard, E. P. Bakkers, and L. P. Kouwenhoven, Science **336**, 1003 (2012).
[44] M. Deng, C. Yu, G. Huang, M. Larsson, P. Caroff, and H. Xu, Nano Lett. **12**, 6414 (2012).
[45] A. Das, Y. Ronen, Y. Most, Y. Oreg, M. Heiblum, and H. Shtrikman, Nat. Phys. **8**, 887 (2012).
[46] H. O. H. Churchill, V. Fatemi, K. Grove-Rasmussen, M. T. Deng, P. Caroff, H. Q. Xu, and C. M. Marcus, Phys. Rev. B **87**, 241401(R) (2013).
[47] A. D. K. Finck, D. J. Van Harlingen, P. K. Mohseni, K. Jung, and X. Li, Phys. Rev. Lett. **110**, 126406 (2013).
[48] S. Vaitiekėnas, Y. Liu, P. Krogstrup, and C. Marcus, Nat. Phys. **17**, 43 (2021).
[49] C. Fasth, A. Fuhrer, L. Samuelson, V. N. Golovach, and D. Loss, Phys. Rev. Lett. **98**, 266801 (2007).
[50] S. Estevez Hernández, M. Akabori, K. Sladek, C. Volk, S. Alagha, H. Hardtdegen, M. G. Pala, N. Demarina, D. Grützmacher, and T. Schäpers, Phys. Rev. B **82**, 235303 (2010).
[51] A. C. Ford, S. B. Kumar, R. Kapadia, J. Guo, and A. Javey, Nano Lett. **12**, 1340 (2012).
[52] D. Liang and X. P. Gao, Nano Lett. **12**, 3263 (2012).
[53] F. Vigneau, V. Prudkovkiy, I. Duchemin, W. Escoffier, P. Caroff, Y.-M. Niquet, R. Leturcq, M. Goiran, and B. Raquet, Phys. Rev. Lett. **112**, 076801 (2014).
[54] E. Halpern, A. Henning, H. Shtrikman, R. Rurali, X. Cartoixa, and Y. Rosenwaks, Nano Lett. **15**, 481 (2015).
[55] Z. Scherübl, G. Fülöp, M. H. Madsen, J. Nygård, and S. Csonka, Phys. Rev. B **94**, 035444 (2016).
[56] A. Iorio, M. Rocci, L. Bours, M. Carrega, V. Zannier, L. Sorba, S. Roddaro, F. Giazotto, and E. Strambini, Nano Lett. **19**, 652 (2018).
[57] B. D. Woods, S. Das Sarma, and T. D. Stanescu, Phys. Rev. B **101**, 045405 (2020).
[58] D. I. Pikulin, J. Dahlhaus, M. Wimmer, H. Schomerus, and C. Beenakker, New J. Phys. **14**, 125011 (2012).
[59] D. Bagrets and A. Altland, Phys. Rev. Lett. **109**, 227005 (2012).
[60] J. Liu, A. C. Potter, K. T. Law, and P. A. Lee, Phys. Rev. Lett. **109**, 267002 (2012).
[61] W. DeGottardi, D. Sen, and S. Vishveshwara, Phys. Rev. Lett. **110**, 146404 (2013).
[62] D. Rainis, L. Trifunovic, J. Klinovaja, and D. Loss, Phys. Rev. B **87**, 024515 (2013).
[63] İ. Adagideli, M. Wimmer, and A. Teker, Phys. Rev. B **89**, 144506 (2014).
[64] B. D. Woods, J. Chen, S. M. Frolov, and T. D. Stanescu, Phys. Rev. B **100**, 125407 (2019).
[65] J. Chen, B. D. Woods, P. Yu, M. Hocevar, D. Car, S. R. Plissard, E. P. A. M. Bakkers, T. D. Stanescu, and S. M. Frolov, Phys. Rev. Lett. **123**, 107703 (2019).
[66] L. A. B. OldeOlthof, J. R. Weggemans, G. Kimbell, J. W. A. Robinson, and X. Montiel, Phys. Rev. B **103**, L020504 (2021).
[67] B. Kalisky, J. A. Bert, B. B. Klopfer, C. Bell, H. K. Sato, M. Hosoda, Y. Hikita, H. Y. Hwang, and K. A. Moler, Nat. Commun. **3**, 922 (2012).
[68] J. S. Lee, B. Shojaei, M. Pendharkar, A. P. McFadden, Y. Kim, H. J. Suominen, M. Kjaergaard, F. Nichele, H. Zhang, C. M. Marcus *et al.*, Nano Lett. **19**, 3083 (2019).
[69] A. Simon and H. G. Von Schnering, J. Less Common Metals **11**, 31 (1966).
[70] H.-J. Meyer, Z. Anorg. Allg. Chem. **620**, 81 (1994).
[71] K. Habermehl and G. Meyer, Z. Naturforsch. B **65**, 770 (2010).

[72] Y. Xu, L. Elcoro, G. Li, Z.-D. Song, N. Regnault, Q. Yang, Y. Sun, S. Parkin, C. Felser, and B. A. Bernevig, arXiv:2111.02433.
[73] Y. Xu, L. Elcoro, Z.-D. Song, M. Vergniory, C. Felser, S. S. Parkin, N. Regnault, J. L. Mañes, and B. A. Bernevig, arXiv:2106.10276.
[74] J. Gao, Y. Qian, H. Jia, Z. Guo, Z. Fang, M. Liu, H. Weng, and Z. Wang, Sci. Bull. **67**, 598 (2022).
[75] H. Wu, Y. Wang, Y. Xu, P. K. Sivakumar, C. Pasco, U. Filippozzi, S. S. Parkin, Y.-J. Zeng, T. McQueen, and M. N. Ali, Nature (London) **604**, 653 (2022).
[76] G. Kresse and J. Hafner, Phys. Rev. B **48**, 13115 (1993).
[77] G. Kresse and J. Furthmüller, Comput. Mater. Sci. **6**, 15 (1996).
[78] J. P. Perdew, K. Burke, and M. Ernzerhof, Phys. Rev. Lett. **77**, 3865 (1996).
[79] Q. Wu, S. Zhang, H.-F. Song, M. Troyer, and A. A. Soluyanov, Comput. Phys. Commun. **224**, 405 (2018).
[80] A. A. Mostofi, J. R. Yates, Y.-S. Lee, I. Souza, D. Vanderbilt, and N. Marzari, Comput. Phys. Commun. **178**, 685 (2008).
[81] See Supplemental Material at http://link.aps.org/supplemental/10.1103/PhysRevLett.132.036601 for more calculation details, which includes Refs. [82,83].
[82] M. A. McGuire, H. Dixit, V. R. Cooper, and B. C. Sales, Chem. Mater. **27**, 612 (2015).
[83] Q. L. He, L. Pan, A. L. Stern, E. C. Burks, X. Che, G. Yin, J. Wang, B. Lian, Q. Zhou, E. S. Choi *et al.*, Science **357**, 294 (2017).
[84] S. Kezilebieke, M. N. Huda, V. Vaňo, M. Aapro, S. C. Ganguli, O. J. Silveira, S. Głodzik, A. S. Foster, T. Ojanen, and P. Liljeroth, Nature (London) **588**, 424 (2020).
[85] C. woo Cho, C. Y. Ng, C. H. Wong, M. Abdel-Hafiez, A. N. Vasiliev, D. A. Chareev, A. G. Lebed, and R. Lortz, New J. Phys. **24**, 083001 (2022).
[86] W. Silvert, J. Low Temp. Phys. **20**, 439 (1975).
[87] A. Luo, Y. Li, Y. Qin, J. Hu, X. Wang, J. Zou, B. Lian, and G. Xu, npj Comput. Mater. **9**, 188 (2023).
[88] W. Dai, A. Richardella, R. Du, W. Zhao, X. Liu, C. Liu, S.-H. Huang, R. Sankar, F. Chou, N. Samarth *et al.*, Sci. Rep. **7**, 7631 (2017).
[89] S. Banerjee, N. Patil, K. Ghosh, S. Saha, G. Menon, S. Ramakrishnan, A. Grover, P. Mishra, T. Chandrasekhar Rao, G. Ravikumar *et al.*, Physica (Amsterdam) **237B**, 315 (1997).
[90] M.-X. Wang, C. Liu, J.-P. Xu, F. Yang, L. Miao, M.-Y. Yao, C. Gao, C. Shen, X. Ma, X. Chen *et al.*, Science **336**, 52 (2012).
[91] M. Sato and Y. Ando, Rep. Prog. Phys. **80**, 076501 (2017).
[92] R. Yu, X. L. Qi, A. Bernevig, Z. Fang, and X. Dai, Phys. Rev. B **84**, 075119 (2011).
[93] A. A. Soluyanov and D. Vanderbilt, Phys. Rev. B **83**, 235401 (2011).
[94] D. Gresch, G. Autes, O. V. Yazyev, M. Troyer, D. Vanderbilt, B. A. Bernevig, and A. A. Soluyanov, Phys. Rev. B **95**, 075146 (2017).
[95] D. Zhong, K. L. Seyler, X. Linpeng, N. P. Wilson, T. Taniguchi, K. Watanabe, M. A. McGuire, K.-M. C. Fu, D. Xiao, W. Yao *et al.*, Nat. Nanotechnol. **15**, 187 (2020).
[96] C. Tang, Z. Zhang, S. Lai, Q. Tan, and W.-b. Gao, Adv. Mater. **32**, 1908498 (2020).
[97] R. White and D. Friedman, J. Magn. Magn. Mater. **49**, 117 (1985).
[98] I. Lyuksyutov and V. Pokrovsky, Adv. Phys. **54**, 67 (2005).
[99] M. Suzuki, H. Muraoka, Y. Inaba, H. Miyagawa, N. Kawamura, T. Shimatsu, H. Maruyama, N. Ishimatsu, Y. Isohama, and Y. Sonobe, Phys. Rev. B **72**, 054430 (2005).
[100] I. F. Lyuksyutov and V. L. Pokrovsky, Mod. Phys. Lett. B **14**, 409 (2000).
[101] M. Sato, Y. Takahashi, and S. Fujimoto, Phys. Rev. B Condens. Matter Mater. Phys. **82**, 134521 (2010).
[102] X.-L. Qi, T. L. Hughes, and S.-C. Zhang, Phys. Rev. B **82**, 184516 (2010).
[103] S.-Q. Shen, *Topological Insulators* (Springer, New York, 2012), Vol. 174.
[104] Z. Zhu, M. Papaj, X. A. Nie, H. K. Xu, Y. S. Gu, X. Yang, D. Guan, S. Wang, Y. Li, C. Liu, J. Luo, Z. A. Xu, H. Zheng, L. Fu, and J. F. Jia, Science **374**, 1381 (2021).